Cancer Research

Targeting a Plk1-Controlled Polarity Checkpoint in Therapy-Resistant Glioblastoma-Propagating Cells

Robin G. Lerner[1], Stefan Grossauer[1], Banafsheh Kadkhodaei[1], Ian Meyers[1], Maxim Sidorov[1], Katharina Koeck[1], Rintaro Hashizume[2], Tomoko Ozawa[1], Joanna J. Phillips[1,3], Mitchel S. Berger[1], Theodore Nicolaides[1,4], C. David James[2], and Claudia K. Petritsch[1,5,6]

Abstract

The treatment of glioblastoma (GBM) remains challenging in part due to the presence of stem-like tumor-propagating cells that are resistant to standard therapies consisting of radiation and temozolomide. Among the novel and targeted agents under evaluation for the treatment of GBM are BRAF/MAPK inhibitors, but their effects on tumor-propagating cells are unclear. Here, we characterized the behaviors of $CD133^+$ tumor-propagating cells isolated from primary GBM cell lines. We show that $CD133^+$ cells exhibited decreased sensitivity to the antiproliferative effects of BRAF/MAPK inhibition compared to $CD133^-$ cells. Furthermore, $CD133^+$ cells exhibited an extended G_2–M phase and increased polarized asymmetric cell divisions. At the molecular level, we observed that polo-like kinase (PLK) 1 activity was elevated in $CD133^+$ cells, prompting our investigation of BRAF/PLK1 combination treatment effects in an orthotopic GBM xenograft model. Combined inhibition of BRAF and PLK1 resulted in significantly greater antiproliferative and proapoptotic effects beyond those achieved by monotherapy ($P < 0.05$). We propose that PLK1 activity controls a polarity checkpoint and compensates for BRAF/MAPK inhibition in $CD133^+$ cells, suggesting the need for concurrent PLK1 inhibition to improve antitumor activity against a therapy-resistant cell compartment. *Cancer Res; 75(24); 5355–66. ©2015 AACR.*

Introduction

Patients with glioblastoma (GBM), the most common and malignant type of brain tumor in adults, have a poor prognosis despite aggressive first-line treatment, which consists of resection followed by radiotherapy with concurrent and adjuvant temozolomide (1). The genetic and phenotypic heterogeneity of GBM poses a major hurdle for the effective treatment of these tumors. Transcriptomic subclassification analyses have revealed discrete molecular subgroups among series of GBM (2, 3), and single-cell RNA sequencing has further demonstrated the presence of multiple molecular subgroups in different cells within a single tumor (4). The intratumoral heterogeneity further manifests as mosaic expression of receptor tyrosine kinases (5, 6), gene copy number variation (7), the presence of multiple genetically distinct clones (8), and the existence of phenotypically distinct tumor-propagating cells (TPC), as highlighted by studies examining the tumorigenicity of xenotransplanted cells sorted from GBM surgical specimen (7, 9, 10). One TPC population of particular interest expresses the cell surface antigen CD133, and $CD133^+$ TPCs were shown to exhibit elevated resistance to standard therapy (11–16). In contrast, NG2 positivity, that is associated with oligodendrocyte progenitor cells (OPC), has been shown to identify TPCs that respond well to chemotherapy (17, 18).

With increasingly routine tumor molecular profiling and the ongoing movement towards the use of targeted therapeutics, it is anticipated that molecular-informed therapeutic decision-making will improve the survival of patients with GBM. Differences between stem and progenitor-like TPCs and other GBM cells could lead to distinct, insufficient responses to those recently emerging targeted therapies and need to be investigated.

Neural stem cells (NSC), OPCs, and TPCs share the ability to undergo asymmetric cell division (ACD). Cells acquiring polarity and as a result segregating cell fate determinants unequally between daughter cells at cytokinesis define ACD. Changes in ACD have been associated with tumor initiation for several cancer types, including GBM (19–21). ACD regulation requires the coordinated activity of a network of polarity regulators and mitotic kinases. This network is well characterized in invertebrate stem cells, and has been shown to include polo kinase (19).

[1]Department of Neurosurgery, Brain Tumor Research Center, University of California San Francisco, San Francisco, California. [2]Feinberg School of Medicine, Northwestern University, Chicago, Illinois. [3]Department of Pathology, University of California San Francisco, San Francisco, California. [4]Department of Pediatrics, University of California San Francisco, San Francisco, California. [5]Helen Diller Comprehensive Cancer Research Center, University of California San Francisco, San Francisco, California. [6]Eli and Edythe Broad Center of Regeneration Medicine and Stem Cell Research, University of California San Francisco, University of California San Francisco, San Francisco, California.

Note: Supplementary data for this article are available at Cancer Research Online (http://cancerres.aacrjournals.org/).

R.G. Lerner and S. Grossauer contributed equally to this article.

Current address for R.G. Lerner: Lancashire Clinical Trials Unit, University of Central Lancashire, Preston, United Kingdom.

Corresponding Author: Claudia K. Petritsch, University of California San Francisco, 1450 Third Street, San Francisco, CA 94143. Phone: 415-476-1636; Fax: 415-514-9792; E-mail: Claudia.petritsch@ucsf.edu

doi: 10.1158/0008-5472.CAN-14-3689

However, for normal mammalian stem and progenitor cells and TPCs, the extent to which polo-like kinase 1 (PLK1; ref. 22), the mammalian homolog of polo kinase, affects ACD is unknown.

Here, we have used human GBM models, to examine ACD in $CD133^+$ versus $CD133^-NG2^+$ cell populations, and to study their response to BRAF/MAPK pathway inhibition. In a subset of malignant astrocytoma the gene encoding cyclin-dependent kinase inhibitor 2A (*CDKN2A*) is deleted, and RAS–RAF–MAPK signaling is constitutively activated due to the $BRAF^{V600E}$ mutation (23). $BRAF^{V600E}$ astrocytoma have been reported to show transient sensitivity to the antitumor effects of the mutant-selective inhibitor vemurafenib, in preclinical (24, 25) and clinical settings (26). On the basis of clinical data from vemurafenib treatment of $BRAF^{V600E}$-melanoma (27), combination therapies are needed to achieve a more durable antitumor effect than $BRAF^{V600E}$/MAPK pathway inhibition alone.

Our data show that $CD133^+$ TPCs display reduced basal proliferation that is less affected by BRAF/MAPK inhibition, in relation to $CD133^-NG2^+$ cells. The lower sensitivity to BRAF/MAPK inhibition is accompanied by increased PLK1 activity and higher rates of polarity and ACD, which can be suppressed by PLK1 inhibition. Combined use of PLK1 and BRAF/MAPK inhibitors increases the antiproliferative and proapoptotic response, especially towards $CD133^+$ cells, and reduces growth of an intracranial $BRAF^{V600E}$-mutant xenograft more effectively than single-agent treatment. The data support the existence of a mitotic polarity/ACD checkpoint in $CD133^+$ TPCs, which is susceptible to PLK1 inhibition. We conclude that investigations into the mechanism of ACD aid in the identification of approaches that support a more durable BRAF/MAPK inhibitor antitumor effect.

Materials and Methods

Immunofluorescence

Tissue sections were generated from 8 GBM that were obtained from consenting patients and distributed anonymously by the Brain Tumor Research Center Repository at the University of California, San Francisco (UCSF, San Francisco, CA). Tissue sections from frozen primary GBM were cut at 5 μm from frozen tissue samples and fixed with 4% paraformaldehyde in PBS (PFA) for 10 minutes at room temperature. Tissue sections from PFA-perfused mouse brains were cut and stained as free-floating 30 μm sections or as 12 μm sections. Cells were pulsed with thymidine analog 5-ethynyl-2′-deoxyuridine (EdU) for 30 minutes at indicated time points, then fixed for 10 minutes with 4% PFA at room temperature. EdU was detected using the Click-it EdU detection kit according to manufacturer's instructions (Life Technologies).

All samples for immunofluorescence were washed with PBS, blocked with PBS+5% normal goat serum for 1 hour at room temperature, and incubated with primary antibody overnight at 4°C (Supplementary Table S1). Samples were washed with PBS and incubated with secondary antibodies for 1 hour at room temperature, washed with PBS+0.2 μg/mL DAPI (to stain nuclei, shown in blue), then with PBS, and mounted with Vectashield (Vecta Labs #H-1000). Quantification of cell counts and immunostainings in tumor sections were performed manually for CD133, NG2, and activated cleaved caspase-3 (CC3), and the number of $Ki67^+$ cells and total cell numbers (DAPI) were counted automatically using ImageJ.

Proliferation assays

Cells from culture or following FACS were plated into black Cell-Bind 96-well plates (Corning #3340) at 500 cells per well in 100 μL of appropriate media ± inhibitors as indicated in figures and legends, with a minimum of 3 technical replicates per condition. At 24, 72, and 120 hours, Alamar Blue (1:10) was added and fluorescence measured (excitation 560 nm, emission 580 nm) after 1 and 3 hours. Fold change was calculated from the vehicle reading taken at 24 hours postplating.

Cell pair and polarity assays

Primary and adherent cell lines were dissociated to single cells, passed through a 70 μm cell strainer, and plated at low density (2,000 cells per 1.9 cm^2 well) onto poly-L-lysine–coated glass coverslips. Cells were allowed to attach or divide (polarity assays; 24 hours, cell pair assays 36–48 hours), inhibitors were added as indicated in figures and figure legends, and cells were fixed and processed for immunofluorescence. For polarity analysis, the sum of the gray values in each of 24 × 15° segments was measured using the Oval Profile plugin for ImageJ, expressed as a percentage of the gray value for each cell, aligned with the maximum at 0° using R, and values averaged across >30 cells per experiment. Cell pairs were scored for asymmetric and symmetric protein distribution as previously described (20).

Cell culture and drug treatment

Primary human GBM cell lines (SF7996, SF8565, proneural subtype) were isolated from surgical specimens obtained through the UCSF Brain Tumor Research Center Biorepository at UCSF (28). Primary cell lines were maintained in ultra low attachment plates (Corning) in Neurobasal-A media (1× B27-A, 1× N2, penicillin/streptomycin (pep/strep), L-glutamine, 10 ng/mL EGF, and 10 ng/mL bFGF2). Primary cells were passaged using Accutase #AM105. DBTRG-05MG and SF188 were obtained from the Nicolaides and Pieper labs at UCSF and were cultured in 10 cm plates (Corning) in DMEM (4.5 g/L glucose, pen/strep, 10% FBS) and passaged using 0.25% trypsin. DBTRG cells were also kept in primary cell conditions to increase the content of $CD133^+$ cells (DBTRG-SF). Cell lines were authenticated by DNA fingerprinting. Cells were treated for 2 hours with vehicle (DMSO) or 5 μmol/L of the actin-organization inhibitor Latrunculin-A (LatA). For Alamar Blue assays, cells were incubated with vehicle, 1 μmol/L PD901, 5 nmol/L BI2536, or a combination of 1 μmol/L PD901 and 5 nmol/L BI2536 for 5 days. DBTRG-05MG cells were treated with vehicle, 1 μmol/L PLX4720, 10 nmol/L BI2536, or a combination of 1 μmol/L PLX4720 and 10 nmol/L BI2536. For desensitization of DBTRG-05M, cells were treated every three days with escalating dosage of PLX4720 up to 6 μmol/L.

Flow cytometry and FACS

Cells were analyzed by flow cytometry using the FACSCalibur. Cell sorting was performed using a BD Biosciences ARIA3 cytometer. For flow cytometry, cells from culture were dissociated by incubating with PBS (Ca^{2+}, MG^{2+}-free) + 0.2 mmol/L EDTA for 10 minutes at 37°C, followed by mechanical dissociation in PBS+0.2 mmol/L EDTA+0.5% BSA (FACS buffer) until a single-cell suspension was achieved. Cells from tumor were dissociated in 20 U/mL papain (Worthington Biochem), followed by antigen recovery by incubation in neurosphere media for 3 hours at 37°C. Alternatively, tumors were dissociated using the neural

stem cell dissociation kit (P; Miltenyi). Live dissociated cells were stained with CD133 and NG2 for 15 minutes on ice, washed in FACS buffer, and stained with secondary antibodies. For phospho-PLK1 (pT120-PLK1) and phospho-ERK (pERK) detection, cells were fixed in 2% PFA and permeabilized using 100% methanol. For FACS, cells were resuspended in FACS buffer containing 0.2 μg/mL DAPI.

Statistical analysis

Appropriate statistical analyses were performed as indicated in figure legends using GraphPad Prism 5.0, Microsoft Excel, or TreeStar FlowJo.

Cell-cycle analysis

Cultured cells were pulsed with EdU (10 μmol/L) for 30 minutes prior to dissociation and processing for FACS. For *ex vivo* analysis of tumor cells, mice were injected with 100 mg/kg EdU 30 minutes to two hours before tumor isolation. DAPI (1 μg/mL) was added to cell suspensions 30 minutes before analysis to measure DNA content.

RNA isolation and qPCR

Total RNA was isolated from FACS-enriched cells or tumor tissue using TRIzol reagent. RNA was reverse transcribed (Life Technologies #4368814), and quantitative real-time PCR performed using Power SYBR qPCR mix (Life Technologies) using an Applied Biosystems 7900HT thermal cycler, with primer sets indicated in Supplementary Table S2. Fold changes were calculated using the $\Delta\Delta C_t$ method (29).

Xenograft models and preclinical treatment

For orthotopic tumor models, 6-week-old athymic mice were implanted with luciferase-expressing DBTRG-05MG cells (3×10^5 cells/mouse) at 1 mm anterior, 2 mm lateral, and 3 mm deep (from Bregma). For flank xenografts, 3×10^7 cells from previous generation flank tumors were harvested and implanted as previously described (25). Tumor growth was measured by bioluminescence imaging and expressed as normalized bioluminescence (fold-change from the start of treatment). Treatment was started at 7 to 21 days postimplantation, and continued for up to 9 days; PLX4720 was injected intraperitoneally at 20 mg/kg daily, whereas BI2536 was injected intraperitoneally at 50 mg/kg twice a week.

Results

CD133 and NG2 identify functionally distinct subpopulations in human GBM

To examine the proportion of CD133- and NG2-positive cells in GBM, we performed coimmunofluorescence on human GBM surgical specimens using CD133 and NG2 antibodies (Fig. 1A). We found the frequencies of CD133 and NG2 cells to be variable between patient samples with CD133 antibody labeling 2% to 20% of tumor cells and NG2 antibody labeling 4% to 23% of the cells (Supplementary Fig. S1A). Less than 20% of $CD133^+$ cells displayed NG2 staining, with $NG2^+$ cells showing a similar low frequency of CD133 costaining, indicating that the markers identify largely nonoverlapping $CD133^+$ and $CD133^-NG2^+$ populations (Fig. 1B and C). In contrast, costaining with NSC marker NESTIN and the OPC marker OLIG2 revealed 83% ± 8% NESTIN positivity of $CD133^+$ cells, and 80% ± 9% OLIG2 positivity of $NG2^+$ cells (Fig. 1B and C). To assess proliferative differences between the two $CD133^+$ and $NG2^+$ populations, we stained specimens for the proliferation marker Ki67 (Fig. 1D), and quantified the proportion of actively cycling cells in each subpopulation. We found that the frequency of actively cycling $NG2^+$ cells was not significantly different from that of bulk tumor cells. We also discovered a significantly lower frequency of Ki67 positivity among $CD133^+$ cells than for $NG2^+$ cells: 11% ± 1% versus 16% ± 2%, respectively (**, $P \leq 0.005$; Fig. 1E).

GBM cell cultures maintain discrete populations of $CD133^+$ and $NG2^+$ cells

We next examined whether the proliferative differences between $CD133^+$ and $NG2^+$ cells remain evident in established GBM cell lines (DBTRG-05MG, aka DBTRG; SF188) and primary GBM cell cultures (SF8565 and SF7996). We used flow cytometry to quantify the frequencies of $CD133^+NG2^-$ (aka $CD133^+$) and $CD133^-NG2^+$ cells. Primary SF7996 and SF8565 cell lines contain a higher proportion of $CD133^+$ cells than established DBTRG and SF188 cell lines. We detected a $CD133^+$ population that was larger than the $CD133^+NG2^+$ population in all cell lines (Fig. 2A and B and Supplementary Fig. S2A and S2B), consistent with results from the analysis of patient tumors.

To further characterize the $CD133^+$ and $CD133^-NG2^+$ cells, we examined FACS-enriched populations as well as unsorted cells for the expression of NSC genes *NESTIN*, *SOX2*, and *MUSASHI1*; the OPC-specific transcription factor *SOX10*; and glial differentiation markers *MBP* and *GFAP*. We found that NSC gene expression is enriched in the $CD133^+$ cells compared with $NG2^+$ cells and unsorted cells, while the *SOX10* expression is enriched in the $NG2^+$ population. Glial differentiation marker expression shows no enrichment in $CD133^+$ cells while in $NG2^+$ cells, MBP expression is elevated (Supplementary Fig. S2C).

To investigate $CD133^+$ cell characteristics *in vitro*, we subjected FACS-enriched $CD133^+$, $CD133^-NG2^+$ cells, and marker-negative cells to Alamar Blue assays. $CD133^+$ cells showed significantly less viability than $CD133^-NG2^+$ and marker-negative cells, the latter two of which were very similar (Fig. 2C).

ACD is elevated in $CD133^+$ GBM cells, in relation to $NG2^+$ cells

Next we examined asymmetric cell divisions (ACD) in $CD133^+$ versus $CD133^-NG2^+$ cells. Immunocytochemistry detecting the subcellular localization of CD133 and NG2 and associated radial profile plots (Fig. 3A and B and Supplementary Fig. S3A) revealed that CD133 protein in $CD133^+$ cells exhibited a more polarized or asymmetric subcellular distribution than NG2 protein in $NG2^+$ cells, which is consistent with the more unequal partitioning of CD133 into daughter cells, as determined by pair assays (Fig. 3C and D and Supplementary Fig. S3B and S3C; ref. 21). Taken together, $CD133^+$ cells consistently exhibited higher rates of polarity and ACD than $CD133^-NG2^+$ cells.

$CD133^+$ cells have differential regulation of cell-cycle dynamics

As ACD and cell-cycle control are tightly linked, we next examined whether $CD133^+$ and $CD133^-NG2^+$ cells exhibit distinct cell-cycle dynamics. Rates at which $CD133^+$ and $CD133^-NG2^+$ cells incorporated EdU were compared, with results indicating that $CD133^+$ cells have an extended G_2–M phase in relation to $CD133^-NG2^+$ and unsorted cells (Fig. 3E and Supplementary Fig. S3D). To distinguish M-phase cells, we stained with the mitotic marker phospho-histone H3 (pHH3). $CD133^+$ cells showed increased pHH3 positivity, in relation to

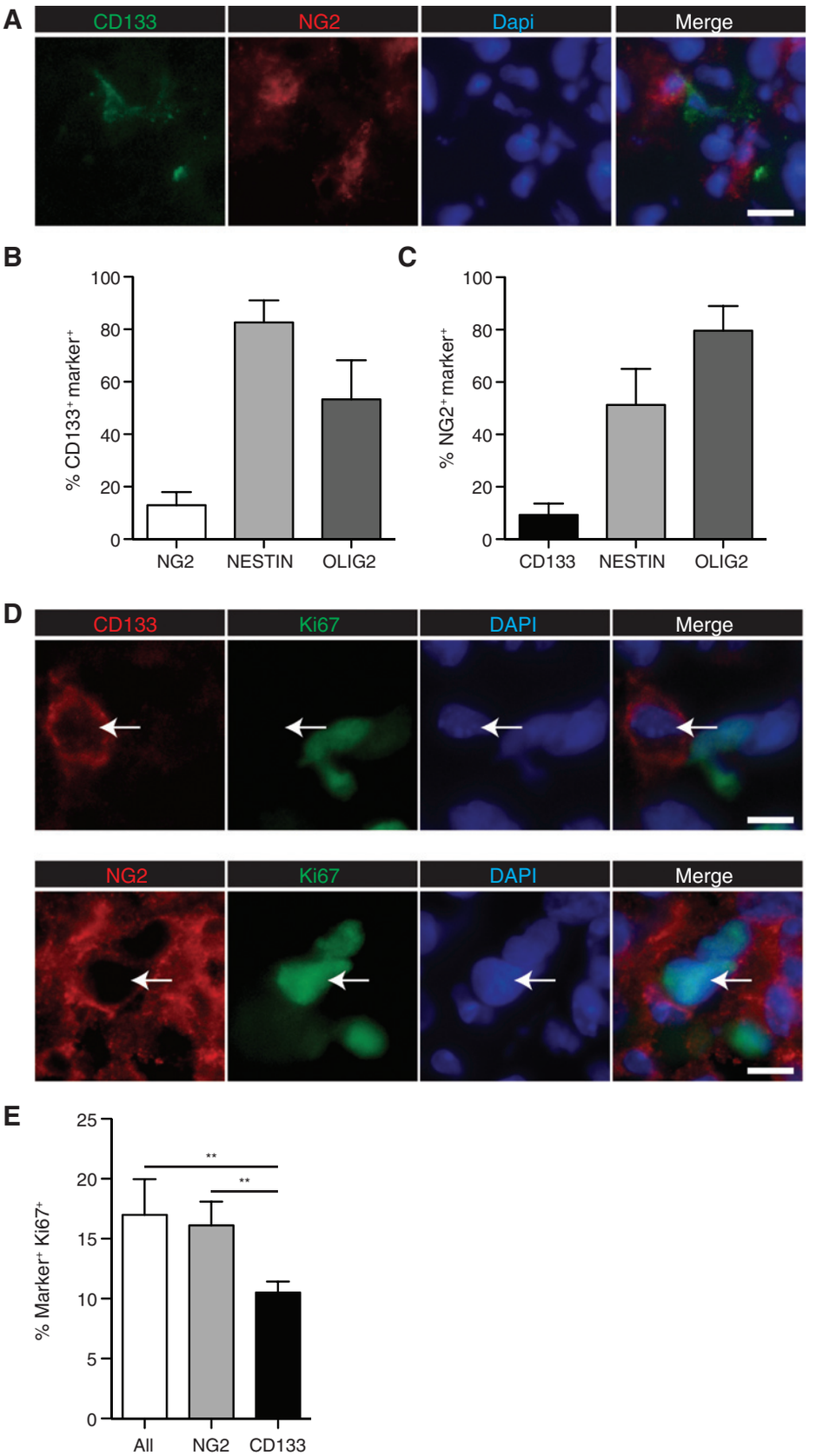

Figure 1.
Proliferation rates and compartment overlap of $CD133^+$ and $NG2^+$ GBMs. A, immunofluorescence image of patient GBM specimen stained with antibodies against CD133 (green) and NG2 (red); DAPI was used to stain DNA (blue). ($N = 8$; error bars, SEM). Quantification of CD133 (B) and NG2 coexpression (C) with NESTIN and OLIG2. A minimum of $n = 77$ cells were counted per tumor, for 8 specimens total. Error bars, SEM. D, coimmunofluorescence of a primary human GBM specimen for CD133 (red, top, arrow), NG2 (red, bottom, arrow), and the proliferative marker Ki67 (green). E, quantification of Ki67 expression in $CD133^+$ and $NG2^+$ cells of primary human GBM specimens. ($N \geq 107$ $CD133^+/NG2^+$ cells counted per tumor from each of 6 specimens; two-tailed t test; error bars, SEM. Scale bars, 20 μm).

$CD133^-NG2^+$ cells (Fig. 3F). However, the fraction of $CD133^+$ cells that stained for pHH3 did not exceed 5% for any cell line, indicating that most G_2–M phase cells, as indicated by EdU incorporation, are in G_2 phase. It is important to note that the higher proportion of G_2–M cells in the $CD133^+$ population merely reflects the prolonged duration of these cell-cycle phases in this population and does not imply overall increased rates of proliferation.

Progression from G_2–M phase occurs, in part, as a result of PLK1 activity (30). PLK1 activation requires Threonine210 (T210) phosphorylation, and pT210-PLK1–directed flow cytometry is used as a surrogate for assessing PLK1 activation. To understand the molecular differences associated with extended G_2–M phase in $CD133^+$ subpopulations, the frequency of $pT210\text{-}PLK1^+$ $CD133^+$ and $NG2^+$ cells was determined by flow cytometry and found to be higher in the $CD133^+$ fraction than in the $CD133^-$ $NG2^+$ or bulk tumor fraction (Fig. 3G). To determine whether PLK1 activation is associated with CD133 polarization, we costained for pT210-PLK1 and CD133. In addition to substantiating PLK1 localization to the centrosome in mitosis (Supplementary Fig. S3E; 22), we detected active PLK1 at the cell periphery, overlapping with CD133 staining (Fig. 3H). On the basis of the totality of these data, we concluded that $CD133^+$ cells differ from autologous $CD133^-NG2^+$ cells by having increased rates of polarized, asymmetric divisions, an extended G_2–M phase and elevated levels of PLK1 activation.

A reciprocal relationship between polarity and PLK1 activity regulates $CD133^+$ cell entry into mitosis

The polarized colocalization of active PLK1 and CD133, as well as elevated PLK1 activity in $CD133^+$ cells and the cell-cycle data, suggests a link between polarity, PLK1 activation and passage through G–M phase. To test this hypothesis, we treated cells with LatA, which is known to disrupt cell polarization by inhibiting actin dynamics (20). We first determined the cellular distribution of CD133 by immunocytochemistry. The effect of LatA was evident by disrupted cellular morphologies with fewer projections and a more rounded appearance. In contrast to control-treated cells, which displayed polarized, membrane-bound CD133, LatA-treated cells showed $CD133^+$ staining as uniformly distributed dots, such that the polarization of CD133 was significantly decreased (Fig. 4A and C and Supplementary Fig. S4A). The localization of NG2, which was largely uniform around the cortex in control cells, showed no significant changes following LatA treatment, except a stronger enrichment at the cortex (Fig. 4B).

We next determined whether LatA treatment alters mitotic entry and PLK activity. To this end, we subjected LatA-treated cells to flow cytometric analysis for pHH3, pT210-PLK1, CD133, or NG2 expression. A decrease in mitotic $CD133^+$ cells, but not $CD133^-$ $NG2^+$ or unsorted cells, was detected following LatA treatment (Fig. 4D and Supplementary Fig. S4B). Depending on the cell line, the frequency of $CD133^+pT210\text{-}PLK1^+$ cells was reduced 2- to 10-fold by LatA treatment (Fig. 4E–H).

Finally, we tested whether PLK1 activity is required for cell polarity by plating cells at clonal densities in the presence of vehicle or the PLK1 inhibitor BI2536 (20, 30). Treated cells were fixed and stained for CD133 (Fig. 4I). Quantification of CD133 polarization revealed that PLK1 inhibition with BI2536 significantly reduced CD133 polarization (Fig. 4J).

We therefore concluded that PLK1 activity, mitotic entry and cell polarization are linked.

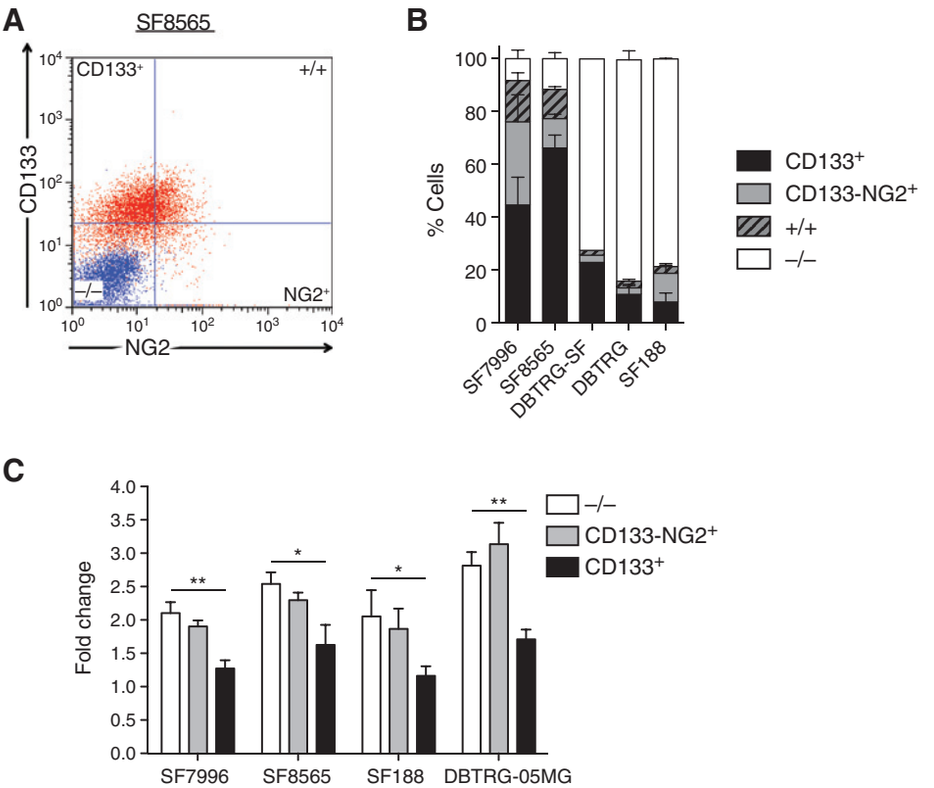

Figure 2.
GBM cell cultures maintain discrete populations of $CD133^+$ and $NG2^+$ cells. A, flow cytometry plot showing CD133 and NG2 expression in SF8565 cell line. The isotype control sample is labeled in blue and antibody-stained samples are in red. B, quantification of frequency of $CD133^+NG2^-$ (CD133), $CD133^-NG2^+$ (NG2), double-positive (+/+), and marker-negative (–/–) cells in SF8565, SF7996, SF188, and DBTRG-05MG cell lines. Error bars, SEM. C, Alamar Blue viability assay of FACS-enriched $CD133^+$ and $CD133^-/NG2^+$ populations from SF7996, SF8565, SF188, and DBTRG-05MG cells. Fold changes in fluorescence after five days of growth demonstrates the lower viability of $CD133^+$ cells compared with $CD133^-/NG2^+$ cells ($n = 3$ individual experiments; one-way ANOVA with Tukey *post hoc* test, error bars, SEM; *, $P \leq 0.005$; **, $P \leq 0.01$).

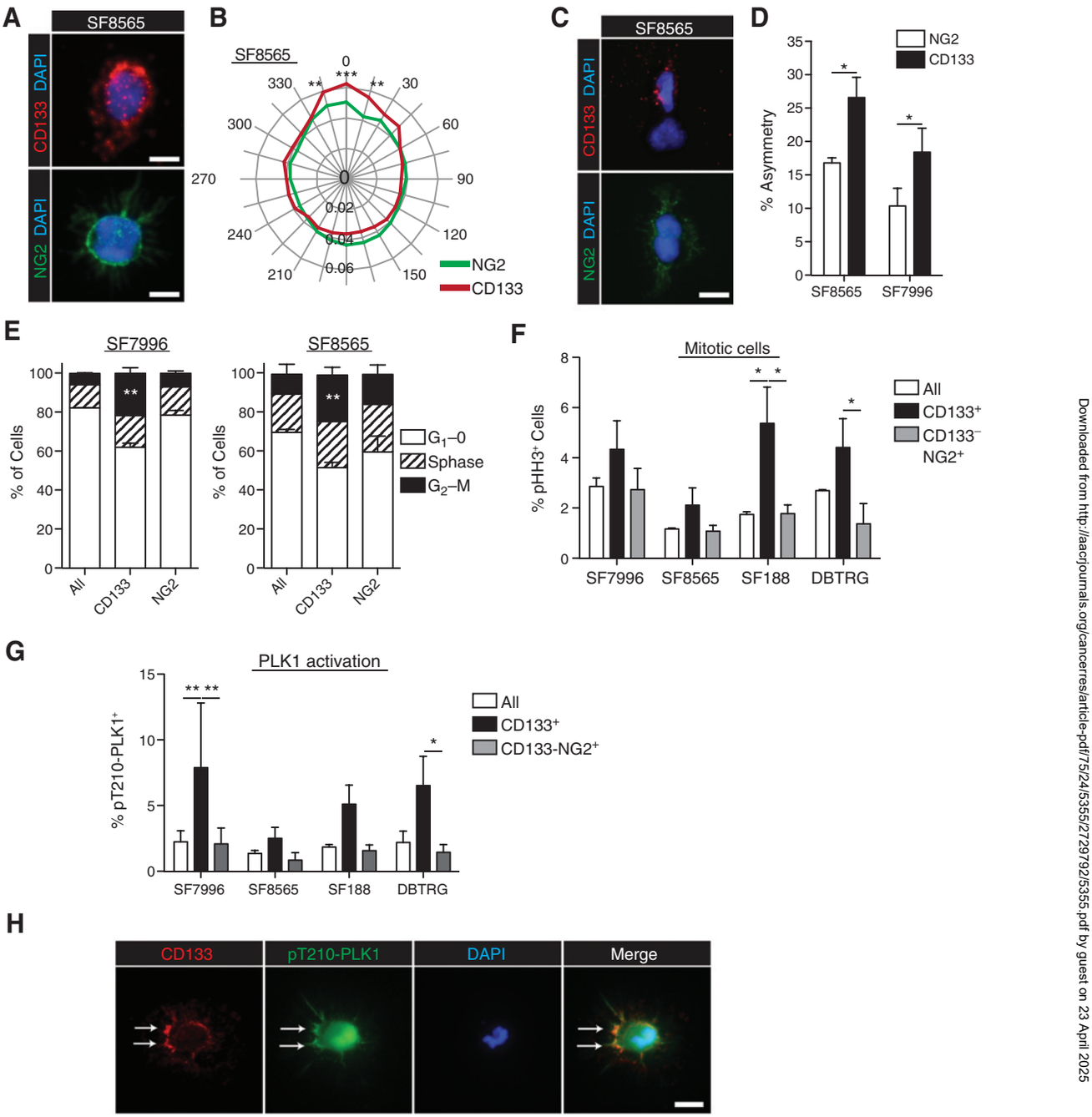

Figure 3.
ACD is elevated and cell cycle dynamics are different in CD133$^+$ cells in relation to NG2$^+$ cells. A, representative image of polarized CD133 localization (red; top), unpolarized NG2 localization (green; bottom), and DAPI (blue; top and bottom), in SF8565 cells (scale bars, 10 μm). B, radial plot showing quantification of CD133 and NG2 polarization. Quantification was performed using the Oval Profile plugin for ImageJ and expressed as a percentage of the gray value for each cell, aligned with the maximum at 0°; values are averaged across ≥30 cells/experiment (two-way ANOVA with Bonferroni *post hoc* test; *, $P \leq 0.05$; **, $P \leq 0.01$; ***, $P \leq 0.001$; error bars, SEM). C, pair assays visualizing the asymmetric distribution of CD133 (red; top), symmetric distribution of NG2 (green; bottom), and DAPI (blue; top and bottom), in SF8565 cells (scale bars, 10 μm). D, quantification of asymmetric division frequency of CD133$^+$ and NG2$^+$ cells from two different cell lines ($n = 4$ individual experiments per cell line; ≥30 cell pairs were scored per experiment; two-way paired *t* test; error bars, SEM; *, $P \leq 0.05$). E, cell-cycle analysis of two different GBM cell lines, stratified by expression of CD133 and NG2, and showing an increase in CD133$^+$ cells in G_2–M phase. NG2, CD133$^-$NG2$^+$ cells ($n = 3$ individual experiments per cell line, two-way ANOVA with Bonferroni *post hoc* test; error bars, SEM; **, $P < 0.005$). F, quantification of flow cytometry analyses to detect pHH3 in cell lines stratified by expression of CD133 and NG2 ($n = 2$ individual experiments; two-way ANOVA with Bonferroni *post hoc* test, error bars, SEM; *, $P < 0.05$). G, flow cytometry analysis to detect activated phospho-PLK1 (pT210-PLK1) in cell lines stratified by expression of CD133 and NG2. CD133$^+$ cells show elevated levels of activated PLK1 ($n = 3$ individual experiments; two-way ANOVA with Bonferroni *post hoc* test, error bars, SEM; *, $P \leq 0.05$; **, $P \leq 0.01$). H, immunocytochemistry to detect phosphorylated form of PLK at T120 residue (pT210-PLK; green), CD133 (red), and DAPI staining (blue). Arrows, enriched localization of activated PLK1 and colocalization with CD133 at the cortex (scale bar, 10 μm).

CD133$^+$ cells are less responsive to targeted inhibition of MAPK signaling pathway

We next determined whether CD133$^+$ cells show differential response to MAPK pathway inhibition. First, Alamar Blue assays were performed on all cell lines to determine an effective dosage for the antiproliferative effect of the MAPK inhibitor PD0325901 (PD901; Supplementary Figs. S5A–S5C and S5E). Similarly, we determined the response of DBTRG

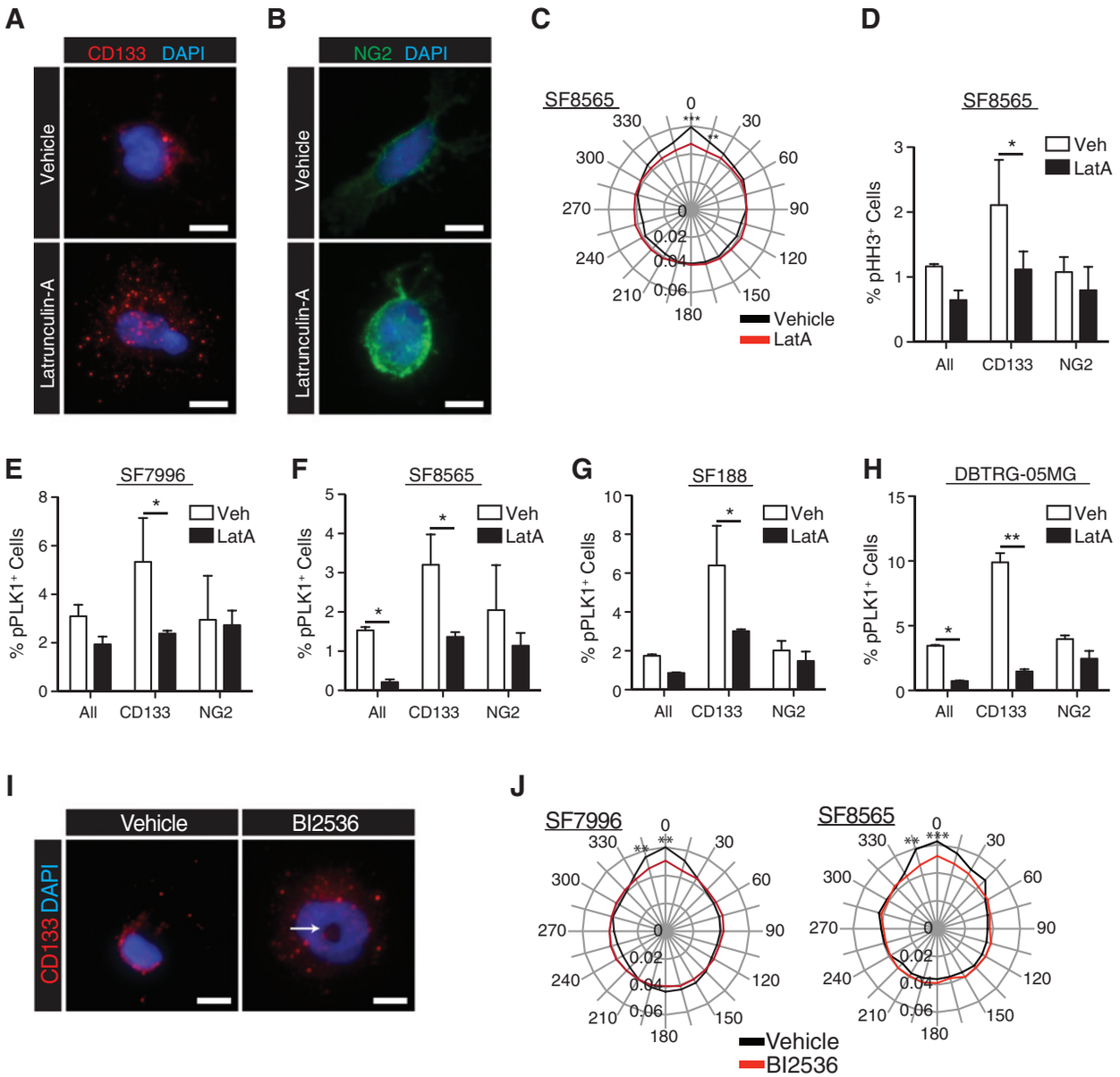

Figure 4.

PLK1 activity controls mitotic entry and cell polarity in CD133$^+$ cells. A, immunocytochemistry to detect CD133 in GBM cells treated with vehicle (DMSO) or Latrunculin-A (LatA; CD133 is in red, DAPI in blue; scale bars, 10 μm). B, immunocytochemistry to detect NG2 in GBM cells treated with vehicle (DMSO) or LatA (NG2 is in green, DAPI in blue; scale bars, 10 μm). C, radial plot showing quantification of polarized CD133 and NG2 distribution in the SF8565 GBM cell line after treatment with vehicle or LatA ($n = 2$ individual experiments per cell line; ≥30 cells were scored per experiment; two-way ANOVA with Bonferroni *post hoc* test; **, $P \leq 0.01$; ***, $P \leq 0.001$). D, flow cytometry analyses quantifying the frequency of pHH3$^+$, mitotic cells in a primary GBM cell line. CD133, CD133$^+$NG2$^-$ cells; NG2$^+$, CD133$^-$NG2$^+$ cells ($n = 3$ individual experiments per cell line; two-way ANOVA with Bonferroni *post hoc* test; error bars, SEM). E–H, flow cytometry analyses quantifying the frequency of pT210-PLK1+ cells (%pPLK1+ cells) in four different cell lines, following treatment with LatA ($n = 4$ individual experiments per cell line; two-way ANOVA with Bonferroni *post hoc* test; error bars, SEM). *, $P \leq 0.05$ in C–H. I, immunocytochemistry for CD133 (red) and DAPI staining (blue) in GBM cells treated with Vehicle or 1 nmol/L BI2536 for 2 hours. Arrow depicts the typical polo arrest phenotype. J, quantification of CD133 and NG2 polarization in vehicle and BI2536–treated (1 nmol/L, 2 hours) GBM cell lines ($n = 2$ individual experiments per cell line; ≥30 cells scored per experiment; two-way ANOVA with Bonferroni *post hoc* test; **, $P \leq 0.01$; ***, $P \leq 0.001$).

cells carrying the $BRAF^{V600E}$ mutation to increasing doses of PLX4720, the vemurafenib tool compound (Supplementary Fig. S5D).

Next we subjected FACS-enriched $CD133^+$, $CD133^-NG2^+$, and marker-negative cells to a viability assay after 5-day treatments with PD901 or PLX4720. PD901 and PLX4720 reduced the viability of $CD133^-NG2^+$ and marker-negative cells, respectively, but exerted no effect on $CD133^+$ cells (Fig. 5A and B). We then assessed the effects of extended drug treatment by propagating cells in the continuous presence of PD901 or PLX4720, and quantifying the frequency of $CD133^+$ and $NG2^+$ cells by flow cytometry at each passage, for up to four passages. During the course of 2 weeks of treatment, the proportion of $NG2^+$ cells decreased by 36% (SF188) and by 43% (DBTRG; Fig. 5C), respectively, while the proportion of $CD133^+$ cells remained unchanged (Fig. 5D).

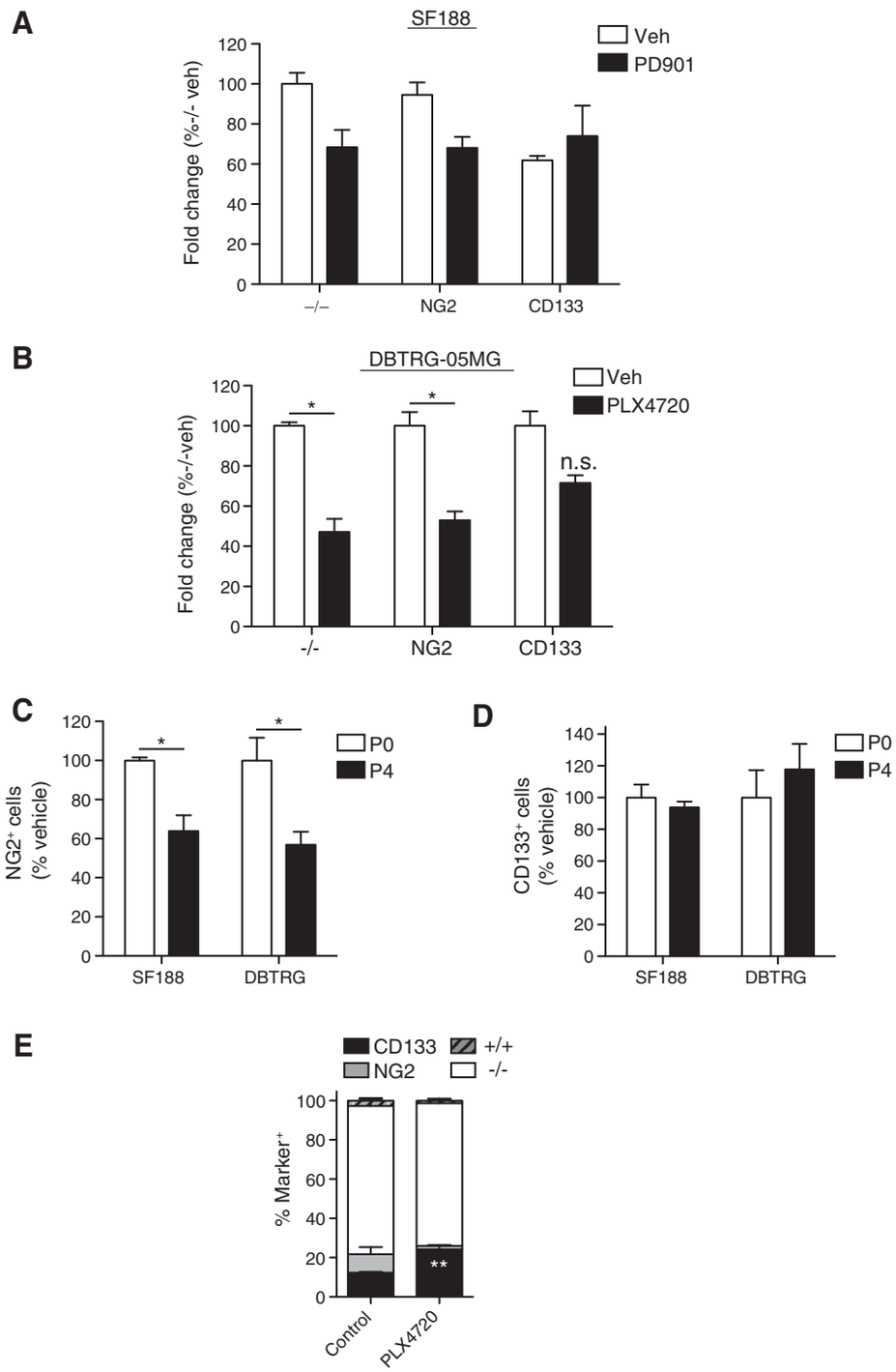

Figure 5.
Decreased sensitivity of CD133+ subpopulations to MAPK pathway inhibition. Alamar Blue viability assay using FACS-enriched $CD133^+$, $NG2^+$, and marker-negative (−/−) cells from SF188 GBM cell lines (A) treated for 5 consecutive days with 0.5 μmol/L PD901 (MAPK inhibitor) and vehicle (Veh) DBTRG-05MG treated for 5 consecutive days with 1 μmol/L PLX4720 and vehicle ($n = 3$ individual experiments per cell line; two-way ANOVA with Bonferroni *post hoc* test; error bars, SEM). Flow cytometry analyses of $CD133^-NG2^+$ (NG2; C) and $CD133^+NG2^-$ (CD133; D) cell frequency in SF188 and DBTRG-05MG GBM cell lines following treatment with 0.5 μmol/L PD901 (SF188) or 1 μmol/L PLX4720 (DBTRG-05MG) for four passages (P0, passage 0; P4, passage 4; $n = 2$ individual experiments per cell line; one-way ANOVA with Tukey post-hoc test; error bars, SEM; *, $P \leq 0.05$ in B and C). E, flow cytometry analyses of $CD133^+$ and $CD133^-NG2^+$ (NG2) cell frequency in subcutaneous DBTRG-05MG xenografts; established tumors were transplanted into new hosts on average every 6 weeks and received 186 days of continuous treatment with vehicle or PLX4720 (10 mg/kg/d). ($N = 4$ individual tumor specimen; two-way ANOVA with Bonferroni *post hoc* test; error bars, SEM; **, $P \leq 0.01$).

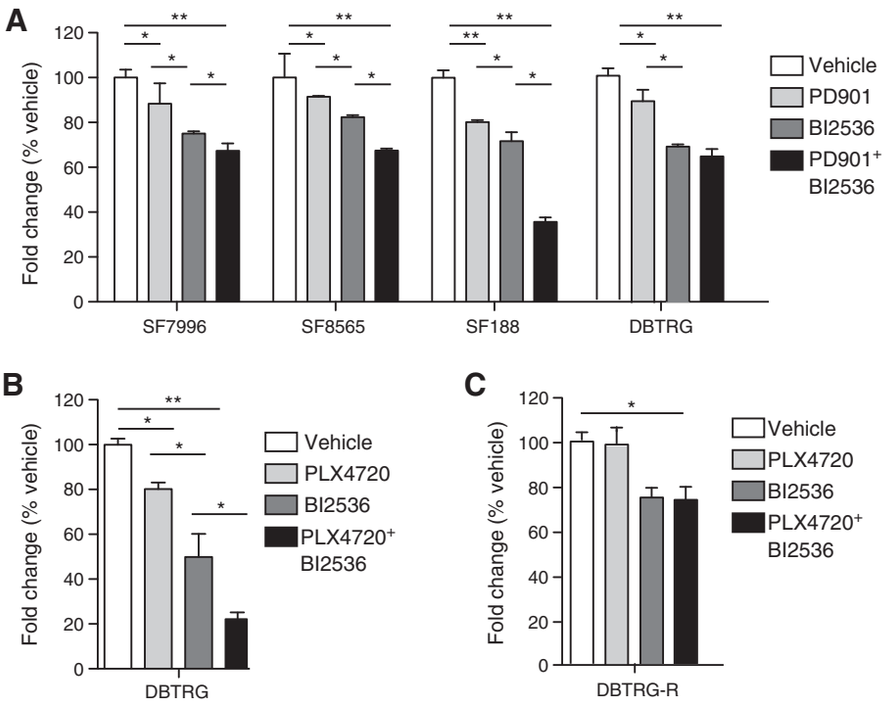

Figure 6.
Targeting PLK1 in combination with BRAF/MAPK inhibition reduces GBM cell viability. A, Alamar Blue viability assay of four GBM cell lines treated with vehicle, 1 μmol/L PD901, 5 nmol/L BI2536, or a combination of PD901 and BI2536 for 5 days ($n = 4$ individual experiments/cell line; error bars, SEM). B, growth assay of DBTRG-05MG cells treated with vehicle, PLX4720, BI2536, or a combination of PLX4720 and BI2536 ($n = 3$ individual experiments/cell line; one-way ANOVA with Tukey *post hoc* tests for A and B; error bars, SEM). C, growth assay of DBTRG-05MG cells pretreated with an escalating dosage of PLX4720, treated with vehicle, PLX4720, BI2536, or a combination of PLX4720 and BI2536 ($n = 3$ individual experiments/cell line; one-way ANOVA with Tukey *post hoc* tests for A and B; error bars, SEM). *, $P \leq 0.05$; **, $P \leq 0.01$ in A and B.

To examine the response of $CD133^+$ cells to MAPK pathway inhibition *in vivo*, subcutaneous DBTRG xenograft tumors were serially propagated in athymic mice that received PLX4720 at 10 mg/kg/d (186 days total treatment). Flow cytometry analysis of disaggregated tumor cells revealed a change in the cellular composition of tumors following extended $BRAF^{V600E}$ inhibition. Whereas $CD133^-NG2^+$ cells were effectively eliminated, the frequency of $CD133^+$ cells was significantly increased (Fig. 5E).

On the basis of these data, we concluded that short-term, intermediate, and chronic BRAF/MAPK inhibition fails to diminish the viability of $CD133^+$ cells.

Targeting PLK1 in combination with BRAF/MAPK inhibition reduces GBM cell growth

Next we assessed whether elevated PLK1 activity provides a point of susceptibility in $CD133^+$ cells, and furthermore tested whether combined PLK1 and BRAF/MAPK inhibition is more effective than BRAF/MAPK inhibition alone at inhibiting tumor cell viability in general and/or in specific cell populations. By itself, PLK1 inhibitor BI2536 (Supplementary Fig. S6A–S6D) blocked viability of unsorted cells in the nanomolar range.

Next, we performed Alamar Blue viability assays on GBM cell lines treated for 5 days with PD901 or PLX4702 alone, or in combination with BI2536. BI2536 decreased viability more substantially than PD901 and PLX4720, in comparing single-agent effects. In all cases, combination treatments inhibited proliferation to a greater extent than any single-agent treatment (Fig. 6A and B). Treatment of DBTRG cells with PLX4720, for an extended length of time and with increasing concentrations of inhibitor, resulted in tumor cell adaptation to inhibitor, such that cell viability in the presence of inhibitor became similar to that of untreated cells. In contrast, BI2536 single-agent treatment of DBTRG showed sustained adverse effect on cell viability (Fig. 6C).

Concurrent inhibition of PLK1 and $BRAF^{V600E}$ has heightened adverse effect on cell viability.

We next examined inhibitor effects on cell subpopulations *in vivo*. Mice with subcutaneous $BRAF^{V600E}$-mutant DBTRG xenograft tumors were treated with PLX4720 or BI2536 alone or in combination. After 5 days treatment mice were injected with EdU and then euthanized, with subcutaneous tumors immediately resected then disaggregated to create cell suspensions for flow sorting. $CD133^+$ and $CD133^-NG2^+$ cells were analyzed for proliferation and cell-cycle effects. Single agent and combination treatments reduced S-phase cells in both $CD133^+$ and $CD133^-NG2^+$ cell populations, with greatest S-phase effect observed for $CD133^+$ cells in tumors exposed to both inhibitors (Fig. 7A). Combination treatment, as well as BI2536 only treatment, significantly increased the number of $CD133^+$ cells in G_2–M, indicative of M-phase arrest (Fig. 7A). Further evidence that BI2536 effectively reaches tumor cells was provided by immunofluorescence of tumor tissue for pHH3, which revealed increased numbers of mitotic cells with abnormally shaped nuclei typically associated with PLK1 inhibition (Supplementary Fig. S7A; ref. 30).

Mice with intracranial xenografts were also treated with inhibitors, alone or in combination, for up to 9 days, to investigate whether an orthotopic microenvironment affects inhibitor activities against their corresponding targets. Dissociated DBTRG tumor cells were examined by flow cytometry for pT210-PLK1 and phospho-ERK (pERK) following PLX4720 and/or BI2536 treatments, with results showing the most substantial decrease in active PLK1 following animal subject treatment with PLK1 inhibitor, alone or with PLX4720 (Supplementary Fig. S7B). In contrast, PLX4720 showed greater inhibitory effect against pERK, an indicator for $BRAF^{V600E}$ (24), than BI2536, with combination PLX4720 + BI2536 showing the most substantial effect in suppressing pERK (Supplementary Fig. S7C). Similar results were

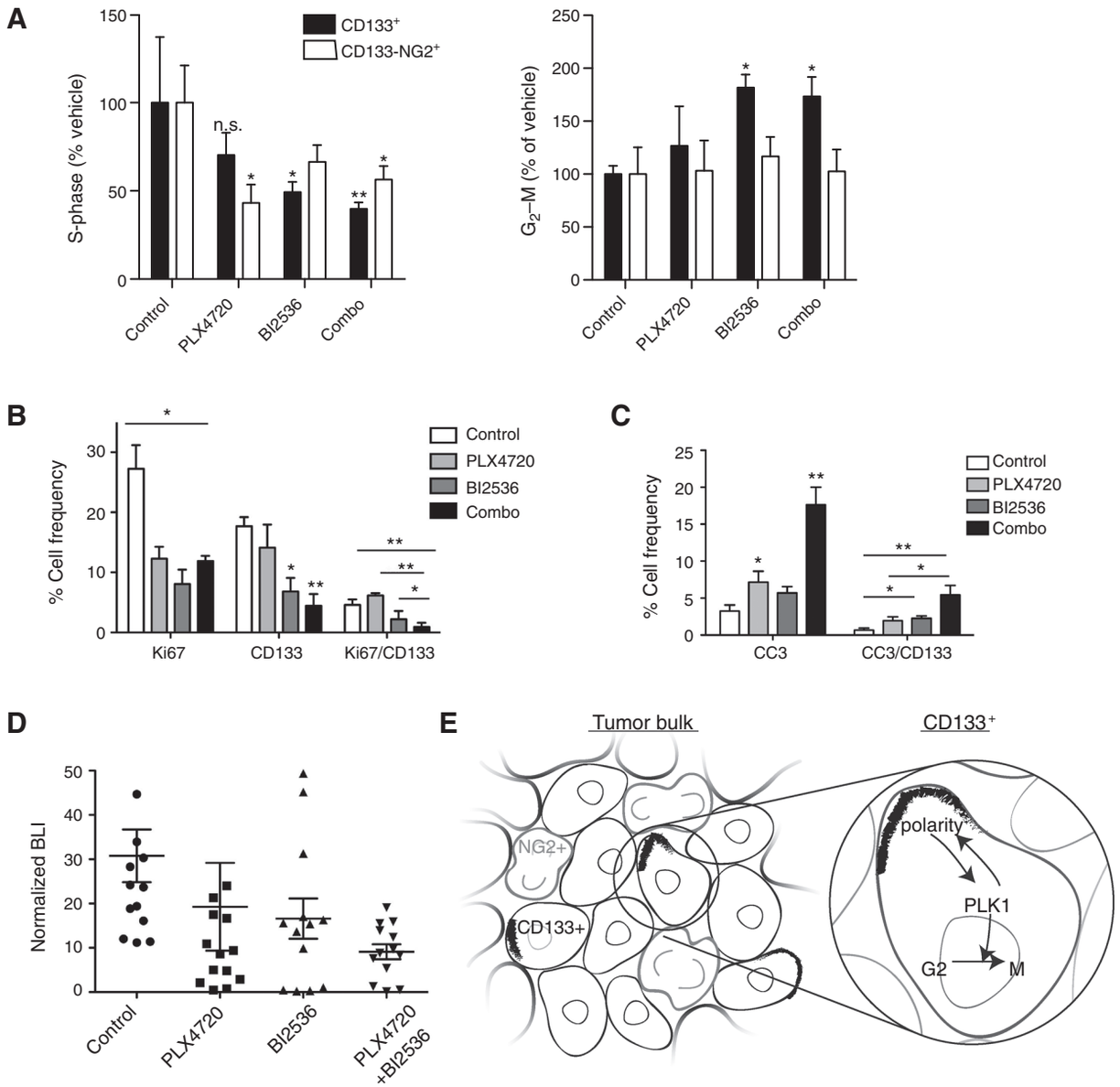

Figure 7.
Effect of combined inhibition of $BRAF^{V600E}$ and PLK1 on $CD133^+$ cells and tumor growth *in vivo*. A, *ex vivo* flow cytometry analyses of subcutaneous DBTRG xenografts treated for 5 days with PLX4720 daily at 20 mg/kg, BI2536 twice at 50 mg/kg or a combination of both inhibitors (Combo). Dissociated tumor cells were analyzed for incorporation of EdU (S-phase) or G_2–M following an EdU pulse 30 minutes before tumors were harvested. ($N = 5$ individual experiments; two-way ANOVA with Bonferroni *post hoc* test, values compared with vehicle treated conditions for each cell type) B, quantification of $Ki67^+$, $CD133^+$, and $CD133^+Ki67^+$ double-positive cells by immunofluorescence performed on intracranial xenograft tumor samples of treated mice. ($N \geq 3$ individual tumors from each treatment group; a minimum of three sections for each treatment group were counted.) C, quantification of cleaved caspase-3 $(CC3)^+$, $CD133^+$, and $CD133^+CC3^+$ double-positive cells by immunofluorescence performed on intracranial xenograft tumor samples of treated mice. ($N \geq 3$ individual tumors from each treatment group; a minimum of three sections for each treatment group were counted). *, $P \leq 0.05$; **, $P \leq 0.005$ in A–C. D, normalized bioluminescence (BLI) readings from intracranial DBTRG-05MG tumors at 7 to 9 days after treatment initiation. Mice were either untreated (control) or treated with either daily PLX4720 at 20 mg/kg, twice-weekly BI2536 at 50 mg/kg, or a combination ($n = 12$–13 animals per treatment group; one-way ANOVA with Tukey *post hoc* test). E, model for a PLK1 inhibitor-sensitive polarity checkpoint in a heterogeneous GBM tumor where $CD133^+$ cells coexist with $CD133^-NG2^+$ ($NG2^+$) cells. $NG2^+$ cells are outlined in gray; polarized CD133 are black crescents.

obtained with MAPK inhibitor PD901 in cells (Supplementary Fig. S7D). A qPCR analysis of CD133 and OPC maker OLIG2 in agent-treated subcutaneous DBTRG xenografts further revealed reduced CD133 expression only after PLK1 inhibition by BI2536 and PLX4720/BI2536 combination treatment (Supplementary Fig. S7E).

Intracranial $BRAF^{V600E}$ xenografts were also examined for treatment effects on $CD133^+$ cell proliferation by Ki67 staining

and apoptosis by cleaved caspase-3 staining, with corresponding results showing combination treatment as producing the most significant antiproliferative response (6-fold vs. control and PLX4720 treated and 3-fold vs. BI2536 treated) towards $CD133^+$ cells (Fig. 7B). The combination treatment also had a strong proapoptotic effect on tumor cells and $CD133^+$ cells in particular (5-fold vs. control and two point 5-fold vs. single agents; Fig. 7C). Antiproliferative and proapoptotic effects were confirmed by bioluminescence imaging of luciferase-modified DBTRG intracranial xenografts, which showed combination therapy as having greatest activity in suppressing tumor growth (Fig. 7D).

Discussion

Recent reports have shown that TPCs are genetically and phenotypically heterogeneous, consisting of populations with distinct responsiveness to therapy (13, 16). These observations have prompted us to perform side-by-side analyses of $CD133^+$ and $NG2^+$ TPC subpopulations for differential response to MAPK pathway inhibition. Consistent with the results of previous studies (31, 32), we determined that autologous $CD133^+$ cells show reduced proliferation in relation to unsorted tumor cells as well as in relation to $CD133^-$ tumor cells, whether in human tumor tissue or cell culture, and irrespective of cell culture conditions (33–35). In contrast, we found $NG2^+$ cells as having very similar proliferation characteristics as bulk, unsorted tumor cells, and that were at higher rates than $CD133^+$ cells.

In addition, our results show distinct cell cycle dynamics and ACD rates, with $CD133^+$ cell characteristics that are reminiscent of the healthy mouse brain, and in which NSCs comprise a partly quiescent population that, when activated to proliferate, predominantly divides asymmetrically (36–38). $NG2^+$ tumor cells, on the other hand, undergo fewer ACD than $CD133^+$ cells and predominantly divide symmetrical, in line with previous data in oligodendroglioma (20). Our findings that $CD133^+$ TPCs are less proliferative while maintaining a higher rate of ACD is consistent with a role for ACD in restricting proliferation.

Many ACD regulators, which have been extensively studied in invertebrates, are conserved in the mammalian genome (19). The activity of one of these, PLK1, is known to increase in G_2 phase of the cell cycle (39). The reciprocal relationship between PLK1 activity and cell polarity, reported in invertebrate model systems (40–42) and shown for the first time here in $CD133^+$ TPCs, suggests a cell-cycle checkpoint in which PLK1 activation and cell cycle G_2–M progression occurs only when appropriate polarity is achieved (Fig. 7E).

The use of chemotherapeutics that disrupt cell polarity could activate this checkpoint, which, in turn, could spare tumor cells from continued cell progression and potential mitotic catastrophe. Through a pharmacologic approach, we have shown that inhibition of this checkpoint not only increases tumor cell apoptosis, especially in the $CD133^+$ subpopulation, but as well limits the proliferation of this important class of TPC.

The discovery of a $BRAF^{V600E}$ mutation in a subset of GBM (23) and encouraging GBM response to $BRAF^{V600E}$ inhibition in preclinical models (24, 25) has prompted ongoing clinical trials for using BRAF inhibitors to treat glioma patients (26, 27). However, preexisting and acquired resistance to $BRAF^{V600E}$ inhibitor is known to occur (43, 44) and as a result several combination therapy approaches are being investigated for increasing the duration and extent of antitumor activity from inhibiting mutant BRAF.

PLK1 is highly expressed in gliomas and GBM (45) and has previously been shown to enhance radiosensitivity in brain tumor models (46). Our discovery that simultaneous MAPK pathway and PLK1 inhibition is especially effective against $CD133^+$ GBM cell subpopulations, which are known to be resistant to routinely used therapies, supports the need to further develop this treatment concept for clinical translation and evaluation in GBM patients.

Disclosure of Potential Conflicts of Interest

No potential conflicts of interest were disclosed.

Authors' Contributions

Conception and design: R.G. Lerner, M. Sidorov, R. Hashizume, C.D. James, C.K. Petritsch

Development of methodology: R.G. Lerner, S. Grossauer, B. Kadkhodaei, M. Sidorov, K. Koeck, R. Hashizume, C.D. James, C.K. Petritsch

Acquisition of data (provided animals, acquired and managed patients, provided facilities, etc.): R.G. Lerner, S. Grossauer, B. Kadkhodaei, I. Meyers, M. Sidorov, K. Koeck, R. Hashizume, C.D. James, C.K. Petritsch

Analysis and interpretation of data (e.g., statistical analysis, biostatistics, computational analysis): R.G. Lerner, S. Grossauer, B. Kadkhodaei, I. Meyers, M. Sidorov, K. Koeck, R. Hashizume, J.J. Phillips, C.D. James, C.K. Petritsch

Writing, review, and/or revision of the manuscript: R.G. Lerner, S. Grossauer, B. Kadkhodaei, M. Sidorov, K. Koeck, M.S. Berger, T. Nicolaides, C.D. James, C.K. Petritsch

Administrative, technical, or material support (i.e., reporting or organizing data, constructing databases): R.G. Lerner, B. Kadkhodaei, K. Koeck

Study supervision: R. Hashizume, T. Ozawa, C.D. James, C.K. Petritsch

Acknowledgments

The authors thank the Pieper, Nicolaides, and Costello labs for cells and Cynthia Cowdrey and the BTRC tissue core for providing tissue sections. For critical discussion, the authors thank M. Oft and the members of the Petritsch lab, S. Mueller, and D. Haas-Kogan. They also thank Y. Yashida, B. Reicholff, N. Andor, M. Kastner, S. Elmes, T. Mazor, R. Santos, H. Collins, and N. Murphy for technical support and C. Crook and H. Oft for volunteering. C.K. Petritsch wishes to dedicate this work to Florian Petritsch.

Grant Support

This work was supported by funding by the NIH/NCI (R01CA164746-04 to C.K. Petritsch), NINDS (RO1NS080619 to C.K. Petritsch and C.D. James), Childhood Brain Tumor Foundation (C.K. Petritsch), Voices against Brain Cancer Foundation (C.K. Petritsch), RAP-Jr. Investigator grant CTSI-UCSF (C.K. Petritsch), the California Institute of Regeneration Medicine (CIRM) TB1-01190 (I. Meyers), the Swedish Society for Medical Research (SSMF) foundation, and the foundation Blanceflor Boncompagni Ludovisi, née Bildt (B. Kadkhodaei).

The costs of publication of this article were defrayed in part by the payment of page charges. This article must therefore be hereby marked *advertisement* in accordance with 18 U.S.C. Section 1734 solely to indicate this fact.

Received December 29, 2014; revised September 1, 2015; accepted September 19, 2015; published OnlineFirst November 16, 2015.

References

1. Weller M, van den Bent M, Hopkins K, Tonn JC, Stupp R, Falini A, et al. EANO guideline for the diagnosis and treatment of anaplastic gliomas and glioblastoma. Lancet Oncol 2014;15:e395–403.
2. Brennan C, Momota H, Hambardzumyan D, Ozawa T, Tandon A, Pedraza A, et al. Glioblastoma subclasses can be defined by activity among signal transduction pathways and associated genomic alterations. PLoS ONE 2009;4:e7752.

3. Verhaak RGW, Hoadley KA, Purdom E, Wang V, Qi Y, Wilkerson MD, et al. Integrated genomic analysis identifies clinically relevant subtypes of glioblastoma characterized by abnormalities in PDGFRA, IDH1, EGFR, and NF1. Cancer Cell 2010;17:98–110.
4. Patel AP, Tirosh I, Trombetta JJ, Shalek AK, Gillespie SM, Wakimoto H, et al. Single-cell RNA-seq highlights intratumoral heterogeneity in primary glioblastoma. Science 2014;344:1396–1401.
5. Snuderl M, Fazlollahi L, Le LP, Nitta M, Zhelyazkova BH, Davidson CJ, et al. Mosaic amplification of multiple receptor tyrosine kinase genes in glioblastoma. Cancer Cell 2011;20:810–7.
6. Szerlip NJ, Pedraza A, Chakravarty D, Azim M, McGuire J, Fang Y, et al. Intratumoral heterogeneity of receptor tyrosine kinases EGFR and PDGFRA amplification in glioblastoma defines subpopulations with distinct growth factor response. Proc Natl Acad Sci U S A 2012;109:3041–6.
7. Piccirillo SGM, Combi R, Cajola L, Patrizi A, Redaelli S, Bentivegna A, et al. Distinct pools of cancer stem-like cells coexist within human glioblastomas and display different tumorigenicity and independent genomic evolution. Oncogene 2009;28:1807–11.
8. Andor N, Harness JV, Mueller S, Mewes HW, Petritsch C. EXPANDS: expanding ploidy and allele frequency on nested subpopulations. Bioinformatics 2014;30:50–60.
9. Singh SK, Clarke ID, Terasaki M, Bonn VE, Hawkins C, Squire J, et al. Identification of a cancer stem cell in human brain tumors. Cancer Res 2003;63:5821–8.
10. Singh SK, Hawkins C, Clarke ID, Squire JA, Bayani J, Hide T, et al. Identification of human brain tumour initiating cells. Nature 2004; 432:396–401.
11. Bao S, Wu Q, McLendon RE, Hao Y, Shi Q, Hjelmeland AB, et al. Glioma stem cells promote radioresistance by preferential activation of the DNA damage response. Nature 2006;444:756–60.
12. Jamal M, Rath B. The brain microenvironment preferentially enhances the radioresistance of CD133+ glioblastoma stem-like cells. Neoplasia 2012;16:6049–59.
13. Chen J, Li Y, Yu T-S, McKay RM, Burns DK, Kernie SG, et al. A restricted cell population propagates glioblastoma growth after chemotherapy. Nature 2012;488:522–6.
14. Bhat KPL, Balasubramaniyan V, Vaillant B, Ezhilarasan R, Hummelink K, Hollingsworth F, et al. Mesenchymal differentiation mediated by NF-κB promotes radiation resistance in glioblastoma. Cancer Cell 2013;24: 331–46.
15. Tamura K, Aoyagi M, Wakimoto H, Ando N, Nariai T, Yamamoto M, et al. Accumulation of CD133-positive glioma cells after high-dose irradiation by Gamma Knife surgery plus external beam radiation. J Neurosurg 2010;113:310–8.
16. Lottaz C, Beier D, Meyer K, Kumar P, Hermann A, Schwarz J, et al. Transcriptional profiles of CD133+ and CD133− glioblastoma-derived cancer stem cell lines suggest different cells of origin. Cancer Res 2010; 70:2030–40.
17. Al-Mayhani MTF, Grenfell R, Narita M, Piccirillo S, Kenney-Herbert E, Fawcett JW, et al. NG2 expression in glioblastoma identifies an actively proliferating population with an aggressive molecular signature. Neuro Oncol 2011;13:830–45.
18. Persson AAI, Petritsch C, Swartling FFJ, Itsara M, Sim FJ, Auvergne R, et al. Non-stem cell origin for oligodendroglioma. Cancer Cell 2010;18:669–82.
19. Gómez-López S, Lerner RG, Petritsch C. Asymmetric cell division of stem and progenitor cells during homeostasis and cancer. Cell Mol Life Sci 2014;71:575–97.
20. Sugiarto S, Persson AI, Munoz EG, Waldhuber M, Lamagna C, Andor N, et al. Asymmetry-defective oligodendrocyte progenitors are glioma precursors. Cancer Cell 2011;20:328–40.
21. Lathia JD, Hitomi M, Gallagher J, Gadani SP, Adkins J, Vasanji A, et al. Distribution of CD133 reveals glioma stem cells self-renew through symmetric and asymmetric cell divisions. Cell Death Dis 2011;2:e200.
22. Takaki T, Trenz K, Costanzo V, Petronczki M. Polo-like kinase 1 reaches beyond mitosis-cytokinesis, DNA damage response, and development. Curr Opin Cell Biol 2008;20:650–60.
23. Schiffman JD, Hodgson JG, VandenBerg SR, Flaherty P, Polley M-YCY, Yu M, et al. Oncogenic BRAF mutation and CDKN2A inactivation is characteristic of a subset of pediatric malignant astrocytomas. Cancer Res 2010;70:512–9.
24. Nicolaides TP, Li H, Solomon DA, Hariono S, Hashizume R, Barkovich K, et al. Targeted therapy for BRAFV600E malignant astrocytoma. Clin Cancer Res 2011;17:7595–604.
25. Huillard E, Hashizume R. Cooperative interactions of BRAFV600E kinase and CDKN2A locus deficiency in pediatric malignant astrocytoma as a basis for rational therapy. Proc Natl Acad Sci 2012;109:8710–5.
26. Robinson GW, Orr BA, Gajjar A. Complete clinical regression of a BRAF V600E-mutant pediatric glioblastoma multiforme after BRAF inhibitor therapy. BMC Cancer 2014;14:258.
27. Chapman PB, Hauschild A, Robert C, Haanen JB, Ascierto P, Larkin J, et al. Improved survival with vemurafenib in melanoma with BRAF V600E mutation. N Engl J Med 2011;364:2507–16.
28. Fouse S, Nakamura JL, James CD, Chang S, Costello JF. Response of primary glioblastoma cells to therapy is patient specific and independent of cancer stem cell phenotype. Neuro Oncol 2014;16:361–71.
29. Livak KJ, Schmittgen TD. Analysis of relative gene expression data using real-time quantitative PCR and the 2(-Delta Delta C(T)) Method. Methods 2001;25:402–8.
30. Steegmaier M, Hoffmann M, Baum A, Lénárt P, Petronczki M, Krssák M, et al. BI 2536, a potent and selective inhibitor of polo-like kinase 1, inhibits tumor growth *in vivo*. Curr Biol 2007;17:316–22.
31. Deleyrolle LP, Harding A, Cato K, Siebzehnrubl FA, Rahman M, Azari H, et al. Evidence for label-retaining tumour-initiating cells in human glioblastoma. Brain 2011;134:1331–43.
32. Richichi C, Brescia P, Alberizzi V, Fornasari L, Pelicci G. Marker-independent method for isolating slow-dividing cancer stem cells in human glioblastoma. Neoplasia 2013;15:840–7.
33. Galli R, Binda E, Orfanelli U, Cipelletti B, Gritti A, De Vitis S, et al. Isolation and characterization of tumorigenic, stem-like neural precursors from human glioblastoma. Cancer Res 2004;64:7011–21.
34. Yuan X, Curtin J, Xiong Y, Liu G, Waschsmann-Hogiu S, Farkas DL, et al. Isolation of cancer stem cells from adult glioblastoma multiforme. Oncogene 2004;23:9392–400.
35. Jin F, Gao C, Zhao L, Zhang H, Wang HT, Shao T, et al. Using CD133 positive U251 glioblastoma stem cells to establish nude mice model of transplanted tumor. Brain Res 2011;1368:82–90.
36. Noctor SC, Martinez-Cerdeno V, Ivic L, Kriegstein AR. Cortical neurons arise in symmetric and asymmetric division zones and migrate through specific phases. Nat Neurosci 2004;7:136–44.
37. Ponti G, Obernier K, Guinto C, Jose L, Bonfanti L, Alvarez-Buylla A. Cell cycle and lineage progression of neural progenitors in the ventricular-subventricular zones of adult mice. Proc Natl Acad Sci U S A 2013;110: E1045–54.
38. Calzolari F, Michel J, Baumgart EV, Theis F, Gotz M, Ninkovic J. Fast clonal expansion and limited neural stem cell self-renewal in the adult subependymal zone. Nat. Neurosci 2015;18:490–2.
39. Bruinsma W, Raaijmakers JA, Medema RH. Switching Polo-like kinase-1 on and off in time and space. Trends Biochem Sci 2012;37:534–42.
40. Rivers DM, Moreno S, Abraham M, Ahringer J. PAR proteins direct asymmetry of the cell cycle regulators Polo-like kinase and Cdc25. J Cell Biol 2008;180:877–85.
41. Noatynska A, Panbianco C, Gotta M. SPAT-1/Bora acts with Polo-like kinase 1 to regulate PAR polarity and cell cycle progression. Development 2010;137:3315–25.
42. Wang H, Ouyang Y, Somers WG, Chia W, Lu B. Polo inhibits progenitor self-renewal and regulates Numb asymmetry by phosphorylating Pon. Nature 2007;449:96–100.
43. Villanueva J, Vultur A, Lee JT, Somasundaram R, Fukunaga-Kalabis M, Cipolla AK, et al. Acquired resistance to BRAF inhibitors mediated by a RAF kinase switch in melanoma can be overcome by cotargeting MEK and IGF-1R/PI3K. Cancer Cell 2010;18:683–95.
44. Holderfield M, Deuker MM, McCormick F, McMahon M. Targeting RAF kinases for cancer therapy: BRAF-mutated melanoma and beyond. Nat Rev Cancer 2014;14:455–67.
45. Dietzmann K, Kirches E, von B, Jachau K, Mawrin C, Von Bossanyi P, et al. Increased human polo-like kinase-1 expression in gliomas. J Neurooncol 2001;53:1–11.
46. Tandle AT, Kramp T, Kil WJ, Halthore A, Gehlhaus K, Shankavaram U, et al. Inhibition of polo-like kinase 1 in glioblastoma multiforme induces mitotic catastrophe and enhances radiosensitisation. Eur J Cancer 2013;49:3020–8.